Dramatically Enhanced Visible-light-responsive H_2 Evolution of $Cd_{1-x}Zn_xS$ *via* the Synergistic Effect of Ni_2P and 1T/2H MoS_2 Cocatalysts①

MA Xiao-Wei[a] LIN Hai-Feng[b] LI Yan-Yan[b②]
WANG Lei[b] PU Xi-Peng[a②] YI Xiu-Jie[a②]

[a] (*College of Materials Science and Engineering, Liaocheng University, Liaocheng* 252059, *China*)
[b] (*Key Laboratory of Eco-chemical Engineering, Taishan Scholar Advantage and Characteristic Discipline Team of Eco-chemical Process and Technology, College of Chemistry and Molecular Engineering, Qingdao University of Science and Technology, Qingdao* 266042, *China*)

ABSTRACT Photocatalytic hydrogen generation from water-splitting holds huge promise for resolving the current energy shortage and environmental issues. Nevertheless, it is still challenging so far to develop non-noble-metal photocatalysts which are efficient toward solar-powered hydrogen evolution reaction (HER). In this work, through an ultrasonic water-bath strategy combined with solvothermal and electrostatic assembly processes, we obtain homogeneous $Cd_{1-x}Zn_xS$–Ni_2P–MoS_2 hybrid nano-spheres consisting of $Cd_{1-x}Zn_xS$ solid solutions decorated by Ni_2P and 1T/2H MoS_2 cocatalysts, which demonstrate excellent activity and stability for visible-light-responsive (λ > 420 nm) H_2 production. Specifically, the $Cd_{1-x}Zn_xS$–Ni_2P–MoS_2 nano-spheres with 2 wt% Ni_2P and 0.2 wt% MoS_2 ($CZ_{0.7}S$–2N–0.2M) exhibit the optimal HER activity of 55.77 mmol·g^{-1}·h^{-1}, about 47 and 32 times more than that of $CZ_{0.7}S$ and Pt–$CZ_{0.7}S$, respectively. The outstanding HER performance of $Cd_{1-x}Zn_xS$–Ni_2P–MoS_2 can be ascribed to the presence of abundant HER active sites in Ni_2P nanoparticles and 1T/2H MoS_2 nanosheets as well as the effective transfer and separation of charge carriers. Moreover, the coupling sequence of cocatalysts in $Cd_{1-x}Zn_xS$–Ni_2P–MoS_2 is found to be critical in the regulation of charge transfer pathways and thus the resultant photocatalytic efficiency. The results displayed here could facilitate the engineering of high-performance photocatalysts employing multi-component cocatalysts for sustainable solar-to-fuel conversion.

Keywords: uniform $Cd_{1-x}Zn_xS$–Ni_2P–MoS_2 nano-spheres, MoS_2 with 1T/2H mixed-phases, photocatalytic H_2 evolution, charge transfer pathways, active sites; DOI: 10.14102/j.cnki.0254–5861.2011–2752

1 INTRODUCTION

Nowadays, it is urgently needed to search for a clean and alternative energy to fossil fuel due to the growing energy shortage and environmental crisises[1]. Hydrogen (H_2) as an emerging energy carrier has recently received considerable attention because of its higher energy density and environmental friendliness[2]. Among various technologies for H_2 production, photocatalytic water-splitting using renewable solar energy is deemed as one of the most promising approaches[3]. For photocatalytic H_2 evolution reaction (HER), the exploitation of high-performance visible-light-responsive photocatalysts is of great importance, which could benefit the efficient utilization of solar energy to speed up the development of H_2 energy. Compared with other semiconducting photocatalysts, CdS has been extensively studied for HER owing to its effective visible-light-absorption and suitable conduction band edge for proton reduction[4]. However, pristine CdS suffers from the fast recombination of charge carriers and photocorrosion problems[5],

Received 2 February 2020; accepted 27 February 2020

① This work was supported by the Foundation of State Key Laboratory of Structural Chemistry (20190021), the National Natural Science Foundation of China (51802170, 21801150, 51772162), the Natural Science Foundation of Shandong Province (ZR2018BEM014, ZR2019JQ14, ZR2019MB001), and the Taishan Scholar Project of Shandong Province

② Corresponding authors. Tel: 17860788571, E-mails: liyanyan6771@163.com, xipengpu@lctu.edu.cn and yixiujie@126.com

which decrease its HER performance significantly. Lately, thanks to their tunable band gap and band structures, the $Cd_{1-x}Zn_xS$ solid solutions have demonstrated enhanced photocatalytic activity and stability toward HER[6]. Therefore, the $Cd_{1-x}Zn_xS$ solid solutions show great promise for the construction of novel photocatalysts with exceptional HER activity.

Recent studies have indicated that[7, 8] hybridizing semiconductor photocatalyst with cocatalysts is an effective means to improve its photocatalytic capability, as a result of the introduction of fruitful active sites as well as the promoted transfer and separation of charge carriers. Commonly, the cocatalysts for CdS-based photocatalysts include noble metals[9], metal oxides and sulfides[10, 11], C_3N_4[12], graphene[13], and so on. Of late, the layered transition-metal chalcogenides (TMCs, such as MoS_2 and WS_2)[14] and transition-metal phosphides (TMPs, like Ni_2P and CoP)[15, 16] have been employed as the photocatalytic cocatalysts to display superior HER performance. It is well known that[17] the MoS_2 possesses two crystal structures, i.e., semiconducting 2H phase and metallic 1T phase, which are formed with the trigonal prismatic and octahedral coordination of Mo and S atoms, respectively. The HER active sites of 2H MoS_2 are only related to its edge sites, while both the basal planes and edge sites of 1T MoS_2 are catalytically active toward H_2 evolution[18]. Hence, 1T MoS_2 has attracted keen interest for HER study in recent years. In addition, TMPs such as Ni_2P exhibits similar electronic structure and HER mechanism as compared with the hydrogenase or metal complex catalysts[19], which endows it with an excellent activity toward H_2 generation. Therefore, the 1T MoS_2 and Ni_2P could serve as ideal cocatalysts for $Cd_{1-x}Zn_xS$ solid solutions to achieve efficient H_2 evolution from solar-powered water-splitting. Nevertheless, the 1T MoS_2 is usually obtained through the ultrasonic exfoliation of lithium-intercalated MoS_2 formed in n-butyllithium solution[17, 20]. Meanwhile, the preparation of Ni_2P requires the use of yellow phosphorus or phosphorization treatment under calcining condition[15, 21]. Consequently, the involved dangerous reagents and cumbersome fabrication processes have restricted the wide application of these two cocatalysts to a large extent. Thus, it is highly necessary to develop safe and facile methods to synthesize the 1T MoS_2 and Ni_2P nanocrystals. On the other hand, it's worth mentioning that for the photocatalyst with multi-component cocatalysts, the coupling sequence of cocatalysts may influence the charge transfer pathways and finally the photocatalytic properties, however, which has still rarely been concerned up to now.

In this work, uniform $Cd_{1-x}Zn_xS$ solid solution nano-spheres were prepared by an ultrasonic water-bath method, which were then coupled by Ni_2P and MoS_2 to form unique $Cd_{1-x}Zn_xS$–Ni_2P–MoS_2 hybrid nano-spheres. The Ni_2P nanocrystals were obtained with an ethylenediamine-assisted solvothermal reaction using nontoxic red phosphorus as P source. Meanwhile, the MoS_2 nanosheets synthesized under solvothermal conditions were composed of 1T and 2H mixed-phases. Under visible-light irradiation, the $Cd_{1-x}Zn_xS$–Ni_2P–MoS_2 demonstrates excellent activity and stability toward photocatalytic H_2 evolution, much superior to that of the Pt–$Cd_{1-x}Zn_xS$, $Cd_{1-x}Zn_xS$–MoS_2 and $Cd_{1-x}Zn_xS$–Ni_2P counterparts, as well as most CdS-based photocatalysts reported previously. In addition, comparative experimental results indicate that the coupling sequence of cocatalysts in $Cd_{1-x}Zn_xS$–Ni_2P–MoS_2 has a significant influence on the migration and separation of charge carriers, which can be rationally optimized to achieve an outstanding HER performance.

2 EXPERIMENTAL

2. 1 Materials

All the chemicals with high purity of analytical grade were purchased from Shanghai Adamas-Beta Reagent Co., Ltd. (China) and were used without further purification.

2. 2 Synthesis of $Cd_{1-x}Zn_xS$ nano-spheres

The $Cd_{1-x}Zn_xS$ nano-spheres were prepared by an ultrasound-assisted water-bath method. Typically, take $Cd_{0.3}Zn_{0.7}S$ for an example, 7 mL 0.1 M $C_6H_5Na_3O_7{\cdot}2H_2O$, 2.5 mL 0.03 M $CdCl_2{\cdot}2.5H_2O$, 2.5 mL 0.07 M $ZnCl_2$, and 10 mL 0.1 M CH_4N_2S aqueous solution were added to 100 mL deionized water to form a homogeneous solution. After that 2 mL $NH_3{\cdot}H_2O$ was mixed into the above solution, which was sealed in a beaker and heated at 50 ℃ for 6 h under ultrasonic water-bath condition. After natural sedimentation for several hours, the product was washed with deionized water and ethanol for several times and then dried in a vacuum oven at 70 ℃ for 6 h.

2. 3 Synthesis of 1T/2H MoS_2 nanosheets

MoS_2 nanosheets with 1T/2H mixed phases were synthesized by a solvothermal method. Specifically, 1 mmol of $MoCl_5$ and 10 mmol of C_2H_5NS were dissolved in 30 mL N,N-dimethylformamide via stirring for 1 h. The solution

was then transferred into a 50 mL Teflon-lined stainless-steel autoclave and then heated at 200 ℃ for 24 h. After being naturally cooled to room temperature, the resulting precipitate was washed with ethanol for three times and dried in a vacuum oven at 70 ℃ for 6 h.

2. 4 Synthesis of $Cd_{1-x}Zn_xS$–Ni_2P hybrid nano-spheres

In a typical procedure, 0.2 g $Cd_{1-x}Zn_xS$ was first dispersed into 20 mL ethylenediamine by ultrasonication for 5 mins. Meanwhile, calculated amounts of $Ni(NO_3)_2·6H_2O$ and red P with the molar ratio of Ni to P being 1:5 were dispersed into 10 mL ethylenediamine after ultrasonication for 30 mins, which were then added into the above suspension and agitated for 1 h. Finally, the mixed suspension was sealed into a 50 mL autoclave and kept at 200 ℃ for 24 h. After reaction, the product was rinsed thrice with ethanol and dried in a vacuum oven at 70 ℃ for 6 h. For the preparation of Ni_2P nanocrystals, the process was similar to that for $Cd_{1-x}Zn_xS$–Ni_2P but without the addition of $Cd_{1-x}Zn_xS$.

2. 5 Synthesis of $Cd_{1-x}Zn_xS$–Ni_2P–MoS_2 hybrid nano-spheres

The $Cd_{1-x}Zn_xS$–Ni_2P–MoS_2 hybrid nano-spheres were prepared through the ultrasonic exfoliation of MoS_2 nanosheets followed by an assembling procedure under agitation. Generally, a certain amount of MoS_2 nanosheets were added into 35 mL N,N-dimethylformamide (filled in a round bottom flask) and sonicated for 3 h to get a homogeneous suspension of exfoliated MoS_2. After this step, 0.2 g $Cd_{1-x}Zn_xS$–Ni_2P was mixed into the MoS_2 suspension through ultrasonication for 10 mins, which was then sealed and stirred for 12 h to complete the adsorption and assembling processes. The $Cd_{1-x}Zn_xS$–Ni_2P–MoS_2 can be obtained after the product was washed with deionized water and ethanol and dried in a vacuum oven at 70 ℃ for 6 h. For comparison, based on the above strategy, the $Cd_{1-x}Zn_xS$–MoS_2 hybrid nano-spheres were fabricated by using $Cd_{1-x}Zn_xS$ to replace $Cd_{1-x}Zn_xS$–Ni_2P. In addition, when $Cd_{1-x}Zn_xS$–MoS_2 was employed as growth substrate, the $Cd_{1-x}Zn_xS$–MoS_2–Ni_2P hybrid nano-spheres were prepared according to the solvothermal method for $Cd_{1-x}Zn_xS$–Ni_2P synthesis.

2. 6 Characterization

The crystal structures of synthesized photocatalysts were determined by powder X-ray diffraction (XRD) using a Bruker Diffractometer (Bruker D8 Advance) with monochromatic Cu-$K\alpha$ radiation (λ = 0.15406 nm). The scanning range was 5～85° and the scanning rate was 0.02°. Ultraviolet-visible (UV-vis) absorption spectra were recorded using a Shimadzu UV 3600 spectrometer. Raman signals were measured on the LabRAM HR Evolution Raman spectrometer with a laser wavelength of 532 nm. The surface morphology of the sample was observed employing a ZEISS MERLIN Compact scanning electron microscope (SEM). The internal structure, crystal lattice, and chemical composition of the catalyst were investigated by the transmission electron microscopy (TEM), high-resolution TEM (HRTEM), dark-field scanning transmission electron microscopy (STEM), and energy-dispersive X-ray spectroscopy (EDX) element mapping measurements carried out by a JEOL JEM-2100F transmission electron microscope. Specific surface area data were obtained from a JW-BK222 auto-adsorption system according to the Brunauer-Emmet-Teller (BET) method. The surface composition and chemical state of photocatalyst were detected by X-ray photoelectron spectroscopy (XPS) using a Thermo Fisher ESCALAB 250 Xi spectrometer with monochromatized Al-$K\alpha$ radiation. The photoluminescence (PL) spectra were collected by a Varian Cary Eclipse Fluorescence spectrophotometer utilizing an excitation wavelength of 365 nm.

2. 7 Electrochemical and photoelectrochemical measurements

The photocurrent response and electrochemical impedance spectroscopy (EIS) tests were performed with a CHI 660E electrochemical workstation, in which the sample, Ag/AgCl, and Pt plate were the working electrode, reference electrode, and counter electrode, respectively. The working electrode was prepared according to the following procedures: firstly, the sample powder was dispersed into an aqueous polyethylene glycol solution by ultrasonication for 30 mins, which was subsequently coated onto a fluorinated tin oxide (FTO) glass with a coating area of 2 cm^2. After that the coated FTO glass was dried naturally and then roasted at 450 ℃ for 1 h under N_2 atmosphere so as to counter the peeling of sample during test. To perform the transient photocurrent measurement, the Na_2S (0.35 M)/Na_2SO_3 (0.25 M) aqueous solution was used as electrolyte and the bias potential was set as 0.5 V. The illumination was furnished by using a 300-W Xe lamp equipped with a 420-nm cutoff filter. On the other hand, the EIS test was carried out using a 0.5 M Na_2SO_4 aqueous solution as the electrolyte, and the EIS spectra were collected with the amplitude of 0.005 V and the frequency of 0.1～10^5 Hz under open circuit potential conditions.

2. 8 Evaluation of photocatalytic hydrogen generation activity

The photocatalytic H_2 evolution reaction was measured by a Labsolar-6A online H_2 evolution and detecting apparatus (Beijing Perfectlight Technology Co., Ltd.). To provide visible-light irradiation, a 300-W Xe lamp equipped with a 420-nm cutoff filter was employed as the light source. For each test, 100 mL aqueous solution containing 0.35 M Na_2S/0.25 M Na_2SO_3 was prepared beforehand, into which 10 mg photocatalyst was then dispersed after ultrasonication for 3 mins. Following this step, the photocatalyst suspension was evacuated to high-vacuum state. The reaction temperature for the H_2 evolution reaction was controlled at 6 ℃ by a thermostatic circulating water pump. In order to study the effect of sacrificial agent on the H_2-evolving activity of photocatalyst, 0.375 M ascorbic acid or 10 vol% lactic acid was used to replace the 0.35 M Na_2S/0.25 M Na_2SO_3 solution. At an interval of 60 mins, the generated H_2 was monitored by a GC-7806 gas chromatograph with a TCD detector. The apparent quantum yield (AQY) for the H_2 evolution reaction can be determined by the following expression:

$$\begin{aligned}\mathrm{AQY} &= \frac{\mathrm{Number\ of\ reacted\ electrons}}{\mathrm{Number\ of\ incident\ photons}} \times 100\% \\ &= \frac{2 \times \mathrm{number\ of\ evolved\ H_2\ molecules}}{\mathrm{Number\ of\ incident\ photons}} \times 100\% \\ &= \frac{2 \times n_{\mathrm{H_2}}}{n_{\mathrm{p}}} \times 100\% \\ &= \frac{2 \times n_{\mathrm{H_2}}}{\frac{P \times t \times \lambda}{h \times c}} \times 100\%\end{aligned}$$

In this formula, $n_{\mathrm{H_2}}$ and n_{p} denote the number of produced H_2 molecules and photons, respectively; P is the light power; t = 3600 s represents the irradiation time; λ = 420 nm means the wavelength of incident light; h = 6.63 × 10^{-34} J·s stands for the Planck constant; and c = 3.0 × 10^8 m·s^{-1} is the light speed.

3 RESULTS AND DISCUSSION

3. 1 Photocatalyst characterization

The preparation procedure of $Cd_{1-x}Zn_xS$–Ni_2P–MoS_2 is schematically illustrated in Fig. 1. Firstly, homogeneous nano-spheres assembled by ultra-small $Cd_{1-x}Zn_xS$ nanocrystals were produced through an ultrasound-assisted water-bath method, where the high-energy chemistry caused by ultrasound was critical to the nucleation, growth, as well as subsequent assembling processes of the product[22, 23]. In the second step, the Ni_2P nanoparticles were anchored onto the $Cd_{1-x}Zn_xS$ nano-sphere surface to form $Cd_{1-x}Zn_xS$–Ni_2P by a solvothermal reaction in ethylenediamine. Finally, the MoS_2 nanosheets possessing 1T/2H mixed-phases synthesized under solvothermal conditions were ultrasonically exfoliated, and then combined with $Cd_{1-x}Zn_xS$–Ni_2P via electrostatic adsorption to form the unique $Cd_{1-x}Zn_xS$–Ni_2P–MoS_2 hybrid nano-spheres.

XRD measurement was carried out to study the crystal structure of photocatalyst. Fig. 2a shows that as the Zn-doping content of $Cd_{1-x}Zn_xS$ solid solutions increases from 0.3 to 0.7, the diffraction patterns of $Cd_{0.7}Zn_{0.3}S$ ($CZ_{0.3}S$), $Cd_{0.5}Zn_{0.5}S$ ($CZ_{0.5}S$), and $Cd_{0.3}Zn_{0.7}S$ ($CZ_{0.7}S$) nano-spheres are all in good consistence with that of the hexagonal phase of CdS (JCPDS Card No. 02-0549). Nevertheless, when the Zn-doping ratio was further raised to 0.9, a small amount of ZnO (JCPDS Card No. 65-3411) was generated in $Cd_{0.1}Zn_{0.9}S$ ($CZ_{0.9}S$) product. According to the solubility diagram reported by Hubert et al.[24], the CdS and ZnS possess much lower solubility as compared with ZnO in ammonia solution. Therefore, in an ammonia solution containing Cd^{2+}, Zn^{2+}, and S^{2-} ions, the $Cd_{1-x}Zn_xS$ solid solutions can be produced more easily than ZnO, while the formation of ZnO might be possible only at a higher Zn^{2+} concentration, matching well with our experimental results. On the other hand, the XRD patterns of individual $CZ_{0.7}S$, MoS_2 and Ni_2P, as well as their composites are also tested as presented in Fig. 2b. Obviously, the diffraction peaks of pure Ni_2P nanocrystals could be assigned to the structure of hexagonal Ni_2P (JCPDS Card No. 65-3544). In comparison with bulk counterpart (JCPDS Card No. 77-1716), the (002) and (004) peaks of synthesized MoS_2 nanosheets were moved toward lower 2θ direction, suggesting that layer-spacing of the latter was expanded[25]. Moreover, we can see after careful comparison that the $CZ_{0.7}S$–0.2 *wt*%MoS_2 ($CZ_{0.7}S$–0.2M), $CZ_{0.7}S$–2 *wt*%Ni_2P ($CZ_{0.7}S$–2N), and $CZ_{0.7}S$–2 *wt*%Ni_2P–0.2 *wt*%MoS_2 ($CZ_{0.7}S$–2N–0.2M) hybrids display the diffraction peaks belonging to the $CZ_{0.7}S$ component, while the signals of MoS_2 and Ni_2P cannot be found from the spectra due to their lower loading amounts (below the XRD detection limit of 5 *wt*%)[26].

UV-vis absorption spectra of the nano-sphere assemblies are exhibited in Fig. 3a. By extending the baseline and linear part of the spectrum curve, the absorption edge can be identified as the wavelength at which the intersection point emerges. The absorption edges are found to be 517.3 nm for

$CZ_{0.3}S$, 501.9 nm for $CZ_{0.5}S$ and 497.7 nm for $CZ_{0.7}S$, respectively. Generally, the bandgap of semiconductor is calculated on the basis of the following equation: $(Ahv)^n = K(hv - E_g)$, where *A* stands for the absorbance, *hv* represents the photon energy, *K* is a constant, E_g denotes the band gap, and *n* equals to 2 for direct bandgap semiconductor and 0.5 for indirect bandgap semiconductor, respectively[27]. As is well known, CdS belongs to the direct bandgap semiconductor[28]. Therefore, the bandgaps of $CZ_{0.3}S$, $CZ_{0.5}S$, and $CZ_{0.7}S$ nano-spheres can be determined using *n* = 2 to be 2.47, 2.53, and 2.55 eV, respectively (Fig. 3b). According to the literatures[4, 29], the bandgap of CdS is ～2.4 eV, which is much lower than that of ZnS (～3.7 eV). As a result, with the increase of Zn-doping amount, the bandgap of $Cd_{1-x}Zn_xS$ solid solutions will be enlarged, leading to the shift of absorption edge toward lower wavelength. In addition, the UV-visible absorption spectra of individual $CZ_{0.7}S$ and MoS_2, as well as the $CZ_{0.7}S$–Ni_2P and $CZ_{0.7}S$–Ni_2P–MoS_2 composites were compared. As shown in Fig. 4, the $CZ_{0.7}S$–2N hybrid displayed a much enhanced light-absorption as compared with pure $CZ_{0.7}S$. Moreover, the light-capture of the product was further improved after the $CZ_{0.7}S$–2N was coated by MoS_2 through an electrostatic assembly process. The superior light-harvesting capability of $CZ_{0.7}S$–Ni_2P–MoS_2 hybrids enables them to generate more charge carriers, benefiting from which the photocatalytic reaction can be facilitated significantly.

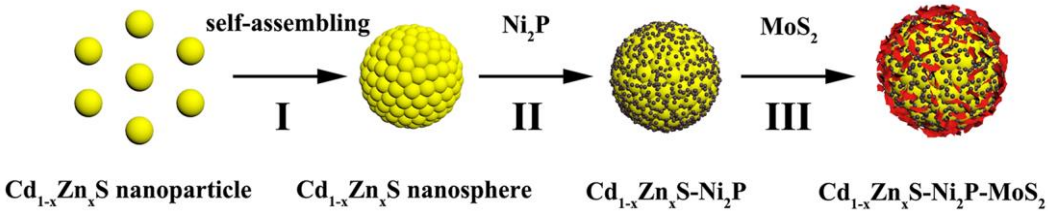

Fig. 1. Schematic illustration for the preparation of $Cd_{1-x}Zn_xS$–Ni_2P–MoS_2 hybrid nano-spheres

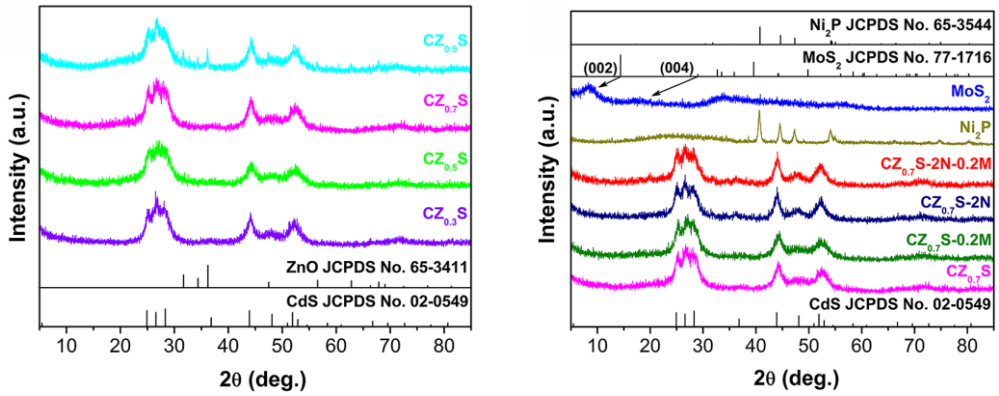

(a) **(b)**

Fig. 2. (a) XRD patterns of $Cd_{1-x}Zn_xS$ solid solutions with different Zn/Cd ratios, (b) XRD patterns of $CZ_{0.7}S$, MoS_2, Ni_2P, $CZ_{0.7}S$–0.2M, $CZ_{0.7}S$–2N, and $CZ_{0.7}S$–2N–0.2M

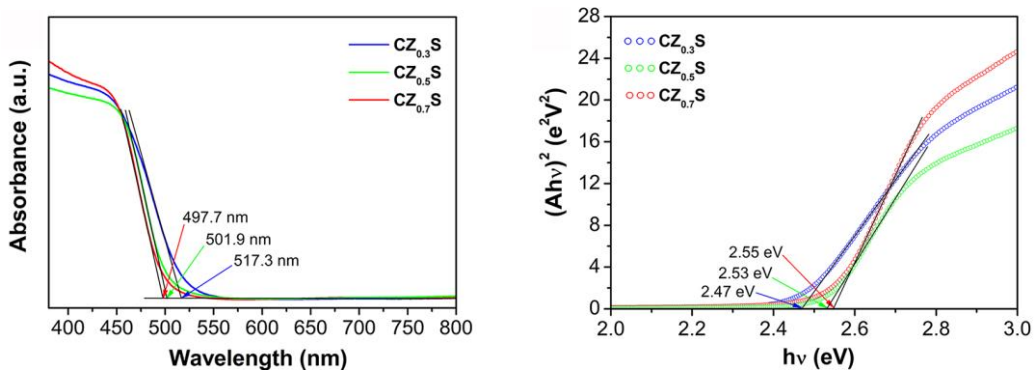

(a) **(b)**

Fig. 3. (a) UV-vis absorption and (b) calculated bandgaps of the $CZ_{0.3}S$, $CZ_{0.5}S$, and $CZ_{0.7}S$ assembled nano-spheres

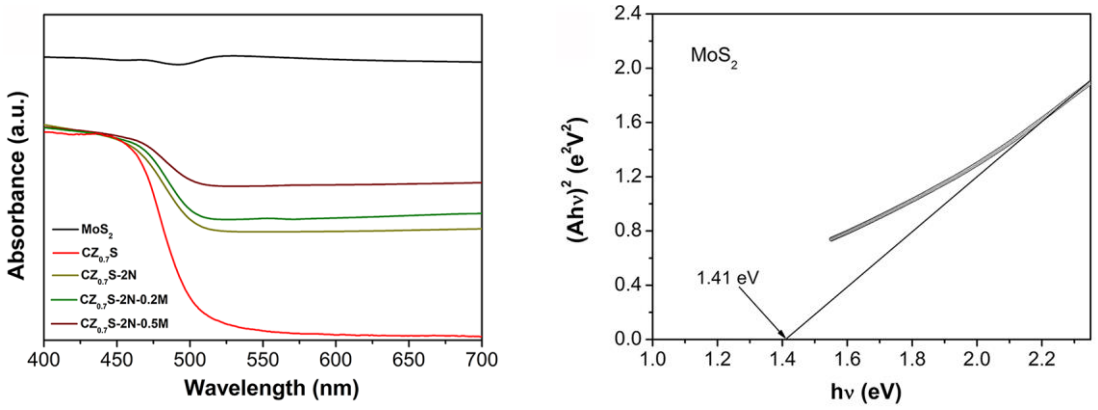

(a) **(b)**

Fig. 4. (a) UV-vis absorption spectra of different samples, (b) Determined bandgap of pure MoS_2 nanosheets

The morphologies of $CZ_{0.5}S$, $CZ_{0.7}S$, and $CZ_{0.9}S$ were disclosed by the scanning electron microscopy (SEM) measurements. As displayed in Fig. 5a～5c, both $CZ_{0.5}S$ and $CZ_{0.7}S$ are featured by uniform nano-sphere architecture, whilst the $CZ_{0.9}S$ sample appears as irregular nanoparticles. According to the size histograms shown in Fig. 5d～5f, the major diameters of $CZ_{0.5}S$ and $CZ_{0.7}S$ are found to be ～85 and 115 nm, respectively. In comparison with $CZ_{0.5}S$ and $CZ_{0.7}S$, the $CZ_{0.9}S$ is provided with a much wider size distribution. On the other hand, the broadened XRD reflections of $CZ_{0.5}S$ and $CZ_{0.7}S$ (Fig. 2a) are indicative of their smaller particle sizes[29]. Correspondingly, the average grain size was calculated using the Scherrer's equation[30] to be merely ～11.5 nm for $CZ_{0.5}S$ and ～13.0 nm for $CZ_{0.7}S$, respectively. Hence, it can be inferred from the above results that the $CZ_{0.5}S$ and $CZ_{0.7}S$ nano-spheres were formed through the assembly of ultra-small primary crystalline grains. Differing from the reported CdS nano-spheres with bigger constituent particles[8, 31], these homogeneous nano-spheres assembled by ultra-small $Cd_{1-x}Zn_xS$ nanocrystals are endowed with more abundant compositions and energy band structures, which enable us more flexibly to mediate their photocatalytic capabilities. Moreover, the rougher surfaces of $Cd_{1-x}Zn_xS$ assembled nano-spheres could furnish more active sites for photocatalytic reactions and more unsaturated atoms to anchor cocatalysts. Therefore, the $Cd_{1-x}Zn_xS$ assembled nano-spheres are anticipated to serve as a desirable photocatalytic material for efficient solar conversion and utilization.

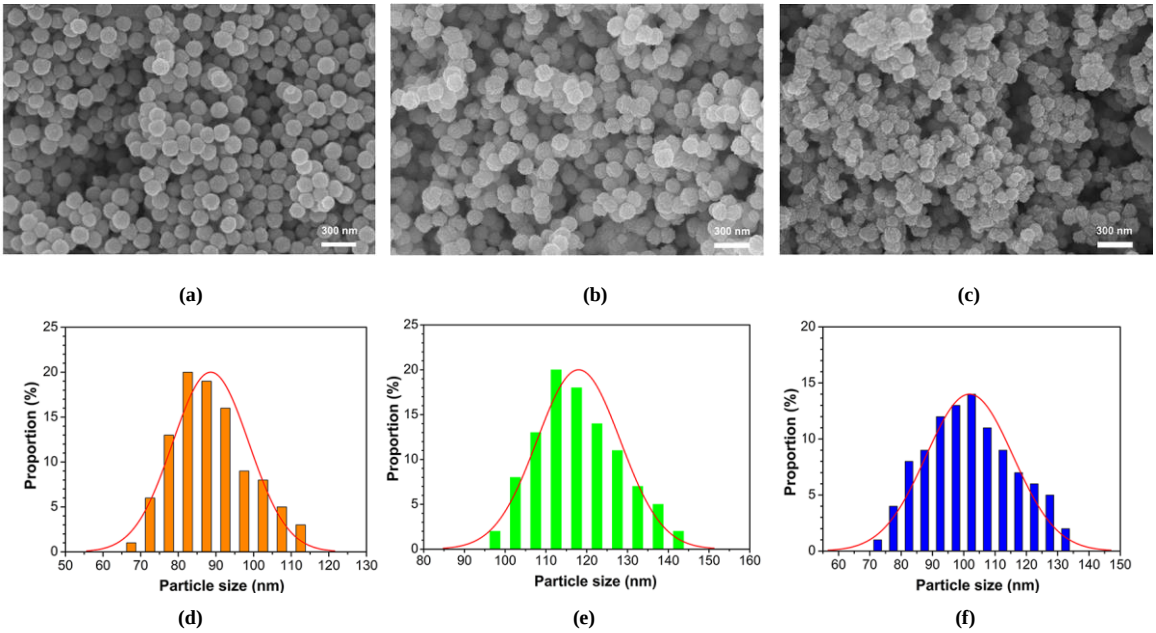

(a) **(b)** **(c)**

(d) **(e)** **(f)**

Fig. 5. (a～c) SEM images and (d～f) Corresponding particle-size distributions of (a, d) $CZ_{0.5}S$, (b, e) $CZ_{0.7}S$, and (c, f) $CZ_{0.9}S$ assembled nano-spheres

Transmission electron microscopy (TEM) images of the $CZ_{0.7}S$ nano-spheres are shown in Fig. 6a and 6b, which display clearly that the nano-spheres are assembled by numerous tiny nanoparticles, agreeing well with the inference based on the SEM observation and particle-size calculation (Fig. 5). Moreover, the high-resolution TEM (HRTEM) graph in Fig. 6c evidences that the $CZ_{0.7}S$ nano-spheres are composed of lots of smaller lattice domains with different orientations, further certifying their assembled architecture. In addition, the dark-field scanning transmission electron microscopy (STEM) photo and corresponding energy-dispersive X-ray spectroscopy (EDX) elemental mapping results of the $CZ_{0.7}S$ nano-sphere are presented in Fig. 6d, which demonstrates the uniform distribution of Zn, Cd and S elements all over the entire nano-sphere. Besides $CZ_{0.7}S$, the $CZ_{0.7}S$–2N–0.2M was also characterized by TEM and HRTEM measurements. It can be seen from Fig. 6e that the $CZ_{0.7}S$–2N–0.2M hybrid possesses homogeneous nano-sphere morphology similar to that of individual $CZ_{0.7}S$. On the other hand, as indicated by the HRTEM result in Fig. 7, the synthesized MoS_2 nanosheets are characteristic of lower crystallinity or even amorphous structure. Thus, the amorphous layers coating on the surface of $CZ_{0.7}S$–2N–0.2M nano-spheres (Fig. 6f, denoted by the yellow dotted ellipses) could be related to the MoS_2 component. Meanwhile, the $CZ_{0.7}S$–2N–0.2M hybrid exhibits the lattice fringes with spacings of 0.22 and 0.35 nm (Fig. 6g), which are attributed to the (111) plane of Ni_2P and (100) plane of $CZ_{0.7}S$, respectively. What's more, the existence of Zn, Cd, Ni, Mo, P, and S elements in $CZ_{0.7}S$–2N–0.2M nano-spheres was confirmed by the STEM and corresponding EDX elemental mapping results in Fig. 6h.

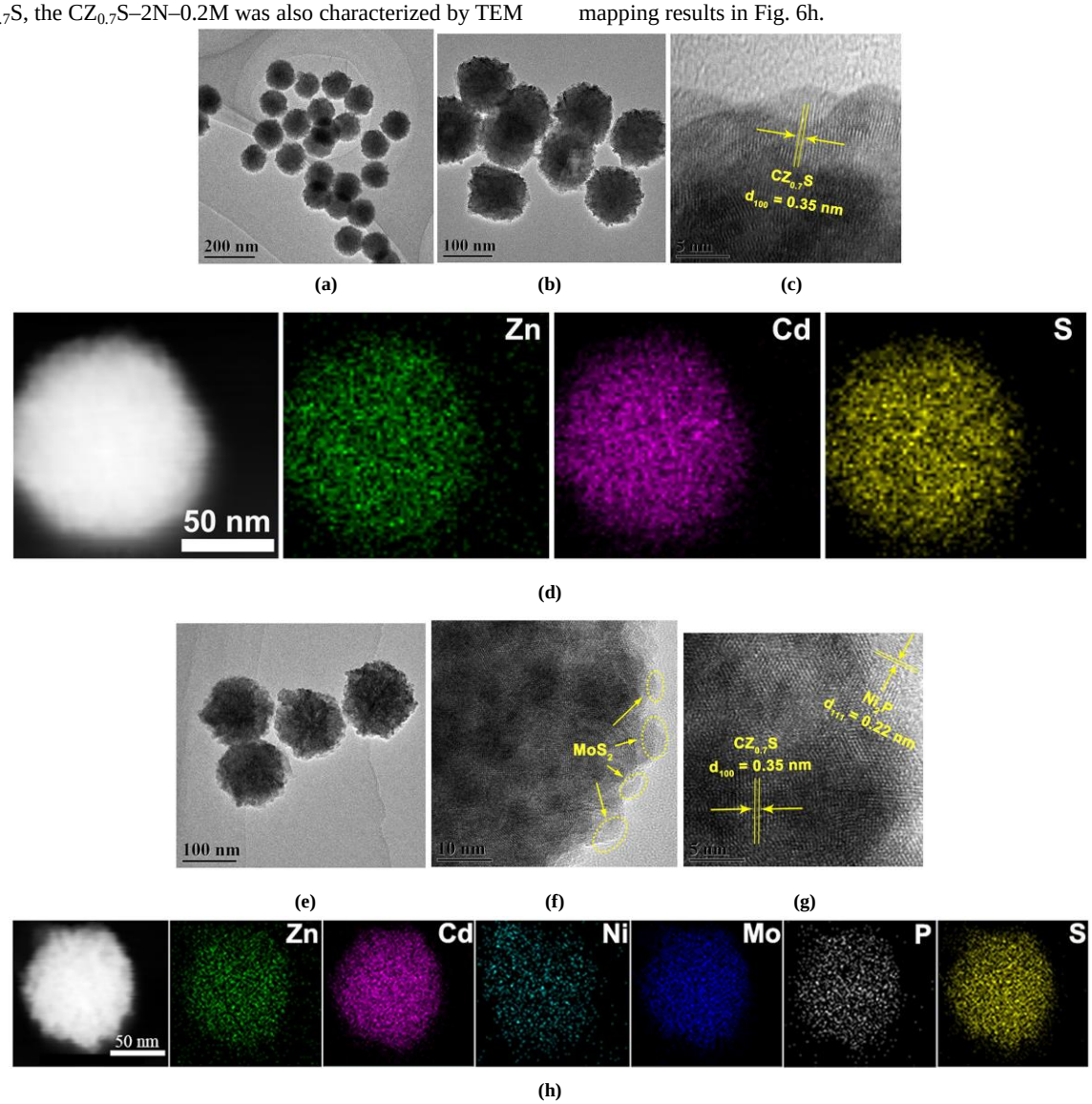

Fig. 6. (a, b) TEM and (c) HRTEM images, as well as (d) Dark-field STEM photo and corresponding EDX elemental mapping results of $CZ_{0.7}S$ nano-spheres, (e) TEM and (f, g) HRTEM graphs, as well as (h) Dark-field STEM image and corresponding EDX elemental mapping results of $CZ_{0.7}S$–2N–0.2M hybrid nano-spheres

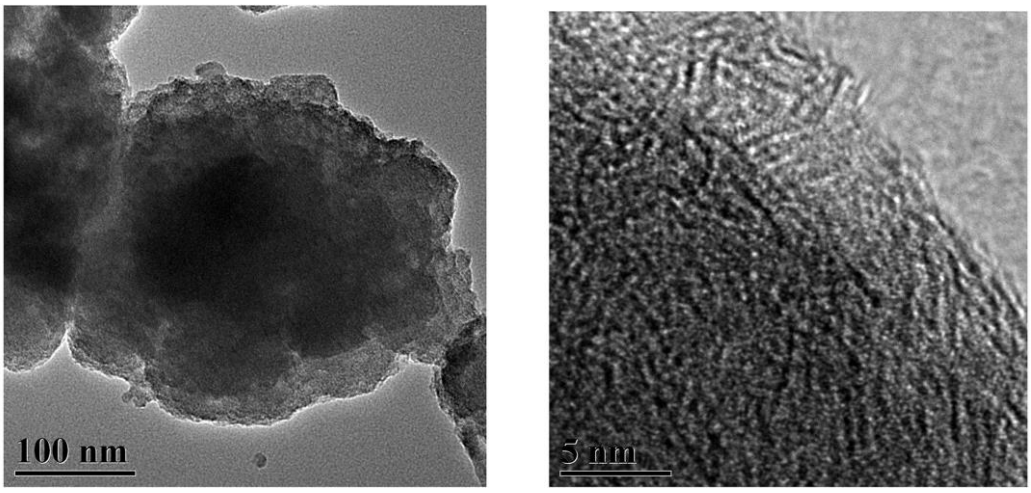

(a) **(b)**

Fig. 7. (a) TEM and (b) HRTEM images of MoS_2 nanosheets

X-ray photoelectron spectroscopy (XPS) measurement was employed to analyze the chemical composition and element valence state of $Cd_{1-x}Zn_xS$–Ni_2P–MoS_2 composite (Here, $CZ_{0.7}S$–2N–5M was taken for an example). As shown in Fig. 8a, for $CZ_{0.7}S$–2N–5M, the Cd $3d_{5/2}$ and $3d_{3/2}$ peaks locate at ～403.7 and ～410.4 eV, respectively, which are associated with the Cd^{2+} species[32]. The Zn $2p_{3/2}$ and $2p_{1/2}$ signals are found to be around 1020.6 and 1043.7 eV (Fig. 8b), respectively, confirming the formation of Zn^{2+} ions[33]. Compared with $CZ_{0.7}$S-2N-5M, the $CZ_{0.7}S$ possesses higher binding energies of Zn 2*p* and Cd 3*d* (1021.5～1044.6 eV and 404.7～411.4 eV) (Fig. 9a and 9b), which suggests that the electron cloud densities of Zn and Cd atoms were increased after $CZ_{0.7}S$ was hybridized by Ni_2P and MoS_2 to produce $Cd_{1-x}Zn_xS$–Ni_2P–MoS_2, indicating the transfer of electrons and formation of heterostructure[34]. Besides, the P 2*p* XPS spectrum is displayed in Fig. 8c, the signal at ～129.5 eV can be attributed to P in Ni_2P, while the other peak situating at ～133.1 eV belongs to a small amount of oxidized P species formed on the surface of catalyst due to exposure to air[35]. We can see from Fig. 8d that Ni 2*p* spectrum exhibits the binding energies of 854.1 ($2p_{3/2}$) and 871.6 ($2p_{1/2}$) eV, which are consistent with that of Ni–P species[36]. Presented in Fig. 8e is the Mo 3*d* XPS spectrum of $Cd_{1-x}Zn_xS$–Ni_2P–MoS_2 hybrid, which comprises three sets of doublet peaks, *i.e.*, 228.0～231.2, 229.2～232.5 and 231.7～234.8 eV, corresponding to the Mo in 1T MoS_2[37], 2H MoS_2[18], and Mo–O species[38], respectively. The Mo signals of individual MoS_2 (Fig. 9c) shift toward higher binding energies when compared to that of $Cd_{1-x}Zn_xS$–Ni_2P–MoS_2 (Fig. 8e), which also verifies the occurrence of electron transfer in the hybrid. On the other hand, in addition to XPS spectrum, the Raman measurement was also carried out to study the phase structure of MoS_2 nanosheets. According to the Raman spectrum in Fig. 8f, the vibration signals appearing at about 281 and 375 cm^{-1} are related to the 2H phase of MoS_2[39], while the signals of 235 and 335 cm^{-1} demonstrate the existence of 1T phase MoS_2[40, 41], in good agreement with the XPS results.

3. 2 Photocatalytic activity

The photocatalytic hydrogen evolution activities of $Cd_{1-x}Zn_xS$–Ni_2P–MoS_2 composites were measured under visible-light (λ > 420 nm) irradiation using Na_2S (0.25 M)/Na_2SO_3 (0.35 M) as sacrificial reagent. Fig. 10a and 10b indicate that the $CZ_{0.7}S$ displays a much better HER activity than the $CZ_{0.3}S$ and $CZ_{0.5}S$ solid solutions. Nevertheless, the $CZ_{0.7}S$ is in possession of decreased light-absorption range (Fig. 3) and BET surface area (due to increased particle-size, Fig. 5) when compared with the latter two. As documented previously, the conduction band minimum potential (E_{CBM}) of a semiconductor (relative to the normal hydrogen electrode, NHE) can be estimated by the empirical formula: $E_{CBM} = \chi - E^c - 0.5E_g$ [6], in which χ represents the electronegativity of a semiconductor, which equals to the geometric mean of absolute electronegativity of the involved atoms. E_g stands for the bandgap of semiconductor, and E^c denotes the energy of free electrons (4.50 eV) on the hydrogen scale. The E_{CBM} for $CZ_{0.3}S$, $CZ_{0.5}S$, and $CZ_{0.7}S$ is calculated to be –0.49, –0.52, and –0.97 V *vs*. NHE, respectively. Therefore, despite of the reduced light-absorption range and BET surface area, the more negative E_{CBM} of $CZ_{0.7}S$ enables it to generate stronger reducing electrons to facilitate HER,

accounting for its superior HER activity than that of $CZ_{0.3}S$ and $CZ_{0.5}S$. Among these $Cd_{1-x}Zn_xS$ solid solutions, the $CZ_{0.7}S$ assembled nano-spheres presented optimal HER activity, which were hence selected as the component to engineer highly-active hybrid photocatalysts toward efficient HER. We can see from Fig. 11a and 11b that MoS_2, $CZ_{0.7}S$ and Pt-loaded $CZ_{0.7}S$ ($CZ_{0.7}S$–1Pt) are all provided with lower activities toward HER. Recent work has demonstrated that Ni_2P can be hybridized with semiconductors to attain a superior photocatalytic activity[42]. Thus, Ni_2P was employed as the cocatalyst of $CZ_{0.7}S$ to enhance its photocatalytic efficiency for HER. Noticeably, after $CZ_{0.7}S$ was combined by Ni_2P to form $CZ_{0.7}S$–Ni_2P hybrids, the HER activity was dramatically improved and the hybrid with 2 *wt*% Ni_2P ($CZ_{0.7}S$–2N) achieved the maximum rate of 34.16 $mmol\cdot g^{-1}\cdot h^{-1}$. In contrast, when the $CZ_{0.7}S$ was supported by 0.2 *wt*% MoS_2 ($CZ_{0.7}S$–0.2M), just a slight increase on the HER rate was observed (Fig. 11b). Moreover, loading 2 *wt*% Ni_2P onto $CZ_{0.7}S$–0.2M ($CZ_{0.7}S$–0.2M–2N) led to a further enhanced HER capability, however, which was much lower than that of $CZ_{0.7}S$–2N. Interestingly, if we loaded 0.2 *wt*% MoS_2 onto $CZ_{0.7}S$–2N ($CZ_{0.7}S$–2N–0.2M) (Figs. 11a and b), its HER rate can be further significantly increased to 55.77 $mmol\cdot g^{-1}\cdot h^{-1}$, about 32 and 47 times more than that of $CZ_{0.7}S$–1Pt and $CZ_{0.7}S$, respectively. The influence of MoS_2 loading amount on the HER activity of $CZ_{0.7}S$–2N–MoS_2 composites was studied. As shown in Fig. 10c, the $CZ_{0.7}S$–2N–0.2M displayed a much higher activity than $CZ_{0.7}S$–2N–0.1M with a reduced MoS_2 content (0.1 *wt*% MoS_2). By increasing the MoS_2 content from 0.2 *wt*% to 0.5 *wt*%, a notable decrease on the HER capability was observed, which may correlate with the excessive MoS_2 that partially screens the light-absorption of $CZ_{0.7}S$, cutting down the amount of charge carrier toward a lowered HER activity. Therefore, it is evident that by employing both Ni_2P and MoS_2 as the cocatalysts of $CZ_{0.7}S$, the coupling sequence has a considerable influence on the HER activity of product and growing Ni_2P onto $CZ_{0.7}S$ followed by MoS_2 coating results in the optimal performance toward HER. In addition, the $CZ_{0.7}S$–2N–0.2M displayed a good HER apparent quantum yield (AQY) of 13.2% at 420 nm (Fig. 10d). The HER activity of $CZ_{0.7}S$–2N–0.2M is better than that of most CdS-based photocatalysts ever reported[13, 43-46]. For one photocatalyst, the stability is a very important aspect in its performance evaluation, except for the photocatalytic activity. Thus, the photocatalytic durability of $CZ_{0.7}S$–2N–0.2M was examined by an uninterrupted HER test for 12 h (Fig. 11c), which demonstrates that the $CZ_{0.7}S$–2N–0.2M is endowed with an exceptional long-term stability toward sustainable H_2 evolution. What's more, the cycling stability of $CZ_{0.7}S$–2N–0.2M was also assessed using the same photocatalyst and testing conditions. From Fig. 11d, we observed that the HER activity of $CZ_{0.7}S$–2N–0.2M experienced no obvious alteration after five repeating measurements, further verifying the outstanding HER stability of $CZ_{0.7}S$–2N–0.2M composite.

In order to investigate the influence of sacrificial agent on the HER activity of $CZ_{0.7}S$–2N–0.2M, lactic acid and ascorbic acid were utilized for the photocatalytic reaction. One can ascertain from Fig. 12a and 12b that both the photocatalytic activities of $CZ_{0.7}S$–2N–0.2M in lactic acid and ascorbic acid aqueous solution were lowered as compared with that in Na_2S/Na_2SO_3 solution. The activity difference of $CZ_{0.7}S$–2N–0.2M in the above three sacrificial agents could be related to their distinct reaction environments. According to the literature[47], the electrochemical potentials of semiconductor conduction and valence bands, water reduction and oxidation, hydroxyl anion, and sacrificial agent oxidation have a linear relationship with the pH of reaction solution. Moreover, the valence band potential of semiconductor can be more positive than the $\cdot OH/^{-}OH$ potential in the solution with very high pH[48]. Consequently, in highly alkaline solution, $\cdot OH/^{-}OH$ redox couple will be produced through the oxidation of hydroxyl anion by photo-excited holes of photocatalyst. The small molecular shuttle $\cdot OH/^{-}OH$ owns higher mobility and oxidizing power, which can efficiently react with the sacrificial agent to inhibit the recombination of charge carriers, leading to a dramatically enhanced HER capability. However, when the photocatalytic reaction was performed in low-pH solution, in comparison with $\cdot OH/^{-}OH$, the slow transfer and subsequent reaction with the scavenger of photogenerated holes results in high charge recombination and decreased photocatalytic activity. In our experiment, the alkaline Na_2S/Na_2SO_3 solution possesses a much higher pH value (～13.5) than that of acidic ascorbic acid (～2.3) and lactic acid (1.4) solutions. Therefore, in Na_2S/Na_2SO_3 solution, the $CZ_{0.7}S$–2N–0.2M could perform photocatalytic HER through the aforementioned redox shuttle mechanism to exhibit an excellent H_2 evolution activity as compared with that in ascorbic acid and lactic acid solutions.

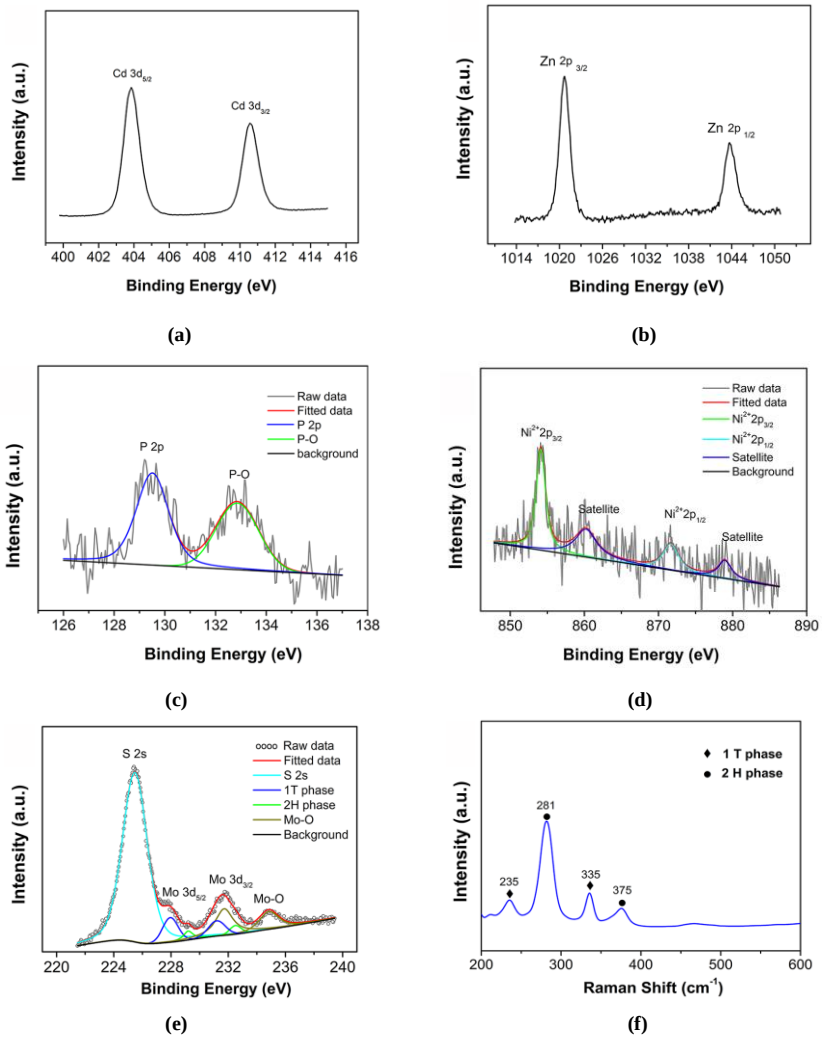

Fig. 8. (a) Cd 3*d*, (b) Zn 2*p*, (c) P 2*p*, (d) Ni 2*p*, and (e) Mo 3*d* XPS spectra of $CZ_{0.7}S$–2N–5M, (f) Raman spectrum of pure MoS_2

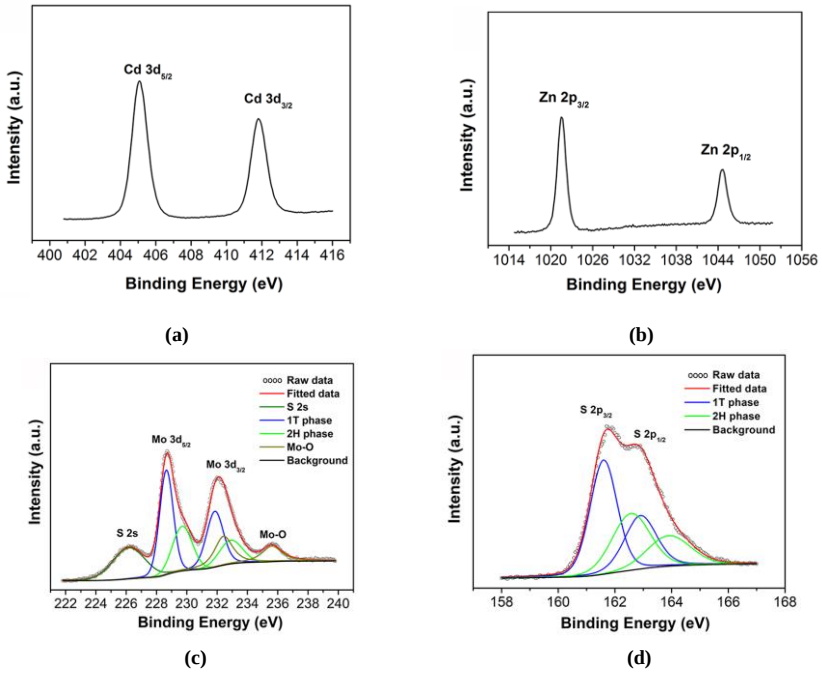

Fig. 9. (a) Cd 3*d* and (b) Zn 2*p* XPS spectra of $CZ_{0.7}S$ nano-spheres, (c) Mo 3*d* and (d) S 2*p* XPS spectra of MoS_2

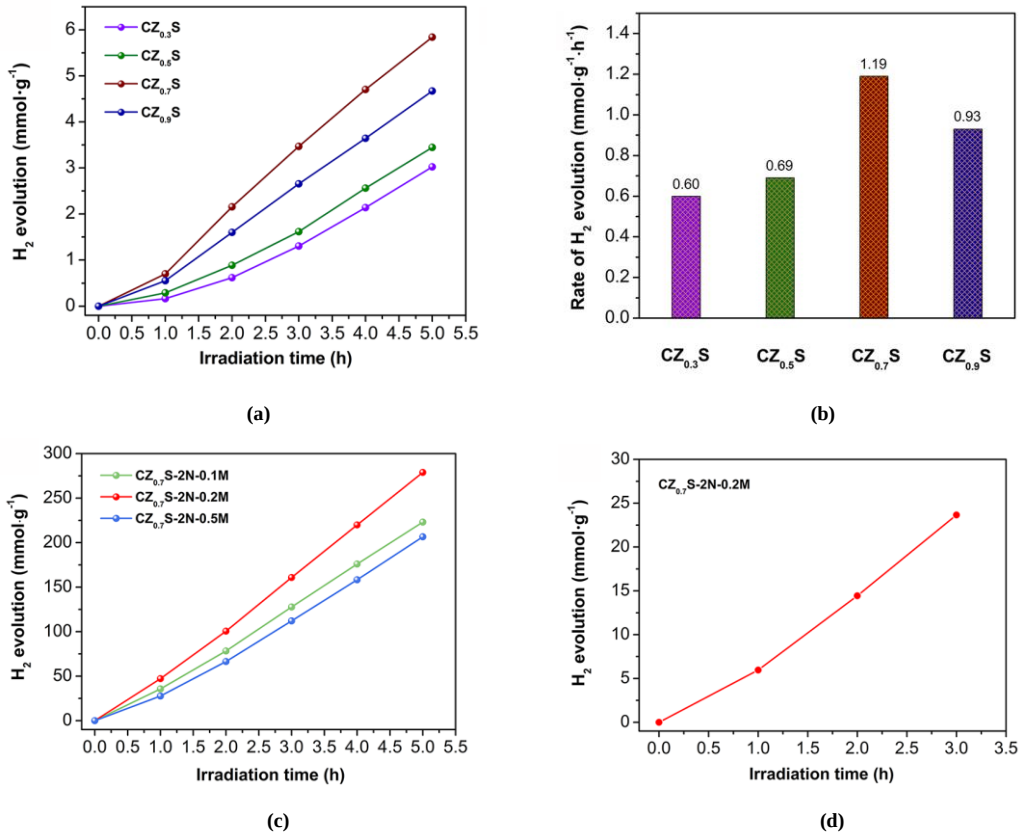

Fig. 10. (a) Photocatalytic H_2 generation activities of $Cd_{1-x}Zn_xS$ solid solutions, (b) Their corresponding average rates, (c) Influence of MoS_2 loading amount on the HER activity of $CZ_{0.7}S$–2N–MoS_2 composites, and (d) H_2 generation curve for calculating the apparent quantum yield (AQY) of $CZ_{0.7}S$–2N–0.2M

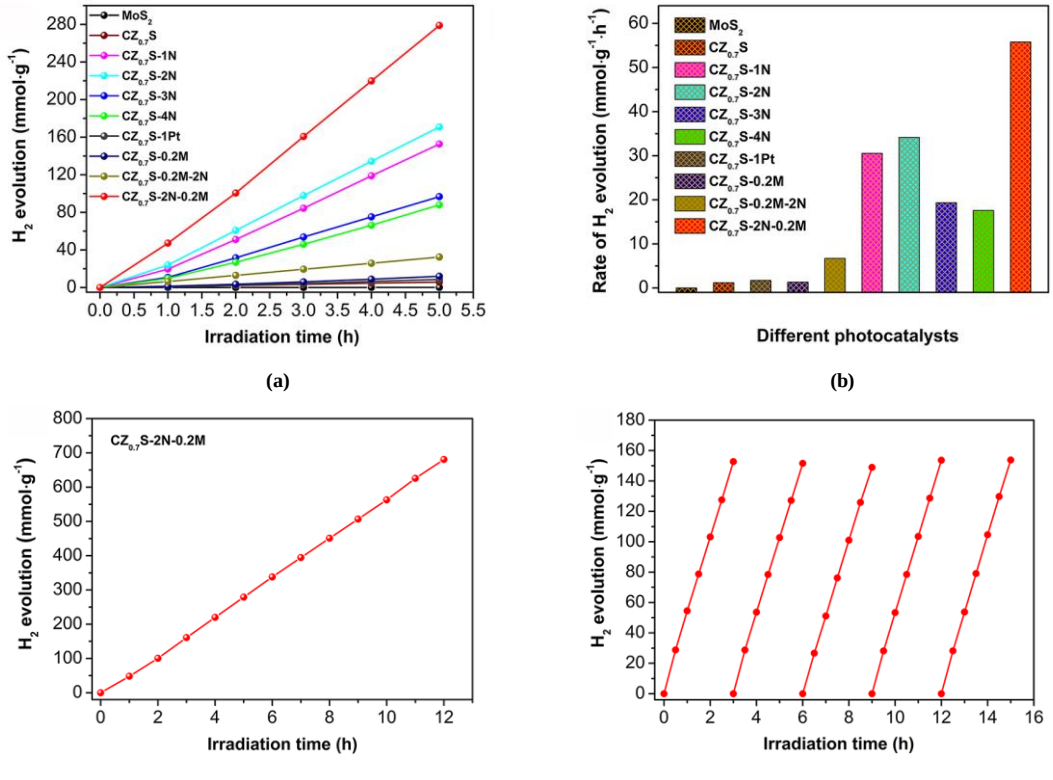

Fig. 11. (a) Visible-light-induced HER activities and (b) Corresponding average rates of different photocatalysts, (c) Long-term H_2 production and (d) Cycling H_2-evolving stability of $CZ_{0.7}S$–2N–0.2M composite

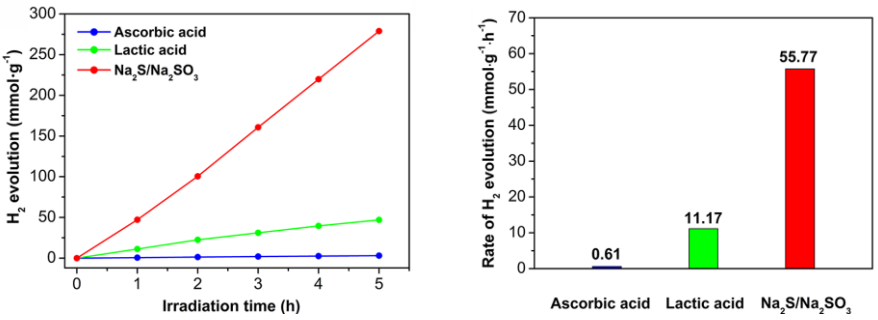

(a) **(b)**

Fig. 12. (a) Photocatalytic HER activities and (b) Corresponding H_2 evolution rates of $CZ_{0.7}S$–2N–0.2M measured using different hole scavengers

3. 3 Photocatalysis mechanism

It is widely acknowledged that[49, 50] in photocatalytic reactions, the transfer and separation processes of charge carriers exert great influence on the overall photocatalytic efficiency. In order to assess the charge separation ability of photocatalyst, the photoluminescence (PL) spectroscopy measurements were carried out. As shown in Fig. 13a, the signals appearing at ～476.5 and 519.5 nm could be attributed to the PL emissions from excitonic and trap-state recombination, respectively[26]. Compared with $CZ_{0.7}S$, the $CZ_{0.7}S$–2N–0.2M hybrid exhibited a lowered PL intensity, which suggests that the separation of electron-hole pairs was promoted by the latter[51], responsible for its excellent HER activity. Moreover, the charge transfer process of photocatalyst was also studied by the electrochemical impedance spectroscopy (EIS) tests. Generally, for a photocatalyst electrode, the semicircular arc diameter of Nyquist curve is in direct proportion to its charge-transfer resistance[52]. Hence, one can see from Fig. 13b that the charge-transfer resistance of $CZ_{0.7}S$–2N–0.2M is much smaller than that of the MoS_2 and $CZ_{0.7}S$ counterparts, which indicates the enhanced capability of $CZ_{0.7}S$–2N–0.2M in the transfer and separation of charge carriers[53], agreeing well with the PL results. In addition, the photocurrent responses of MoS_2, $CZ_{0.7}S$ and $CZ_{0.7}S$–2N–0.2M were compared as displayed in Fig. 13c. In consistence with the PL and EIS analyses, the higher photocurrent density of $CZ_{0.7}S$–2N–0.2M than MoS_2 and $CZ_{0.7}S$ suggests that the $CZ_{0.7}S$–2N–0.2M possesses a better ability in decreasing the recombination of photogenerated charges[33].

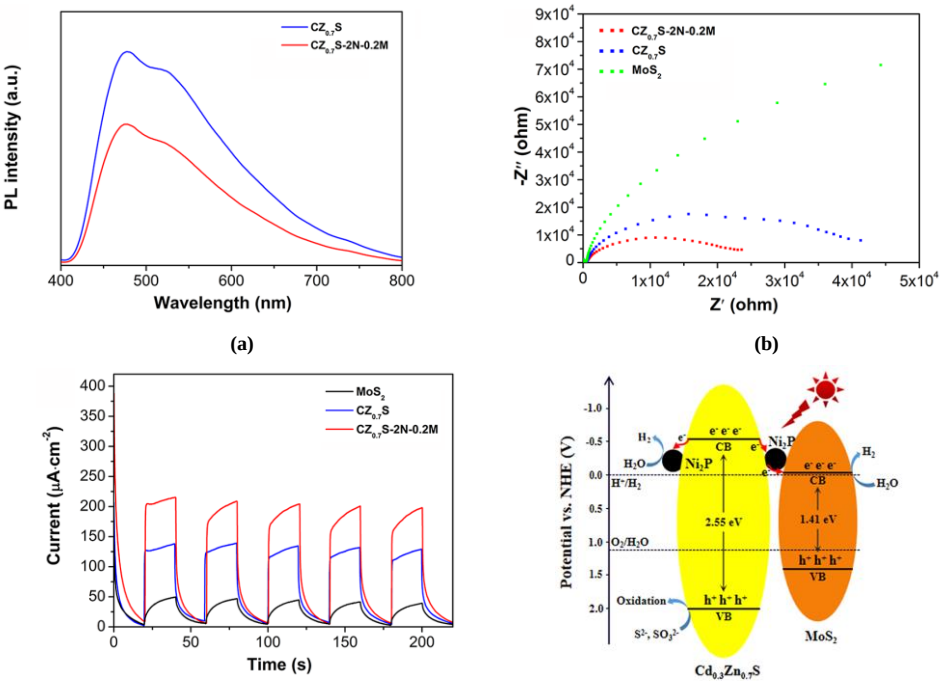

(a) **(b)**

(c) **(d)**

Fig. 13. (a) PL spectra, (b) EIS Nyquist plots, (c) Photocurrent responses of MoS_2, $CZ_{0.7}S$, and $CZ_{0.7}S$–2N–0.2M, and (d) Schematic energy band structures of MoS_2, Ni_2P, and $CZ_{0.7}S$

The significant difference between the HER activities of $CZ_{0.7}S$–2N–0.2M and $CZ_{0.7}S$–0.2M–2N implies that there might exist distinct charge transfer mechanisms in these two composites prepared with opposite coupling sequence of the Ni_2P and MoS_2 cocatalysts. To clarify the mechanism for charge transfer, the energy band structures of $CZ_{0.7}S$ (2.55 eV, Fig. 3b), Ni_2P, and MoS_2 (1.41 eV, Fig. 4b) were schematically illustrated in Fig. 13d. For $CZ_{0.7}S$–Ni_2P–MoS_2, under light-irradiation, the photogenerated electrons could first migrate from the conduction band (CB) of $CZ_{0.7}S$ to the Fermi level of metallic Ni_2P[36, 54], resulting in the spatial separation and remarkably inhibited recombination of charge carriers. Subsequently, the electrons captured by Ni_2P will quickly move to the adjacent MoS_2 due to the higher conductivity of Ni_2P[21]. What's more, the Ni_2P and defective 1T/2H MoS_2 cocatalysts are in possession of a large number of active sites for HER[55, 56]. Hence, benefiting from the effective separation of charge carriers and presence of abundant active sites, the $CZ_{0.7}S$–2N–0.2M is provided with an excellent activity toward photocatalytic H_2 evolution. In comparison with $CZ_{0.7}S$–2N–0.2M, the charge transfer in $CZ_{0.7}S$–0.2M–2N follows a quite different pattern. As MoS_2 was loaded onto $CZ_{0.7}S$ prior to Ni_2P, the photo-excited electrons in $CZ_{0.7}S$ will transfer into the CB of MoS_2 before further flowing into Ni_2P, while the holes left in $CZ_{0.7}S$ valence band (VB) could be injected spontaneously into the VB of MoS_2[57]. Unfortunately, the type-I charge transfer between $CZ_{0.7}S$ and MoS_2 could cause the detrimental recombination of electron-hole pairs. Meanwhile, the oxidizing power of photogenerated holes is lowered after the migration process. As a result of the above two negative factors, the $CZ_{0.7}S$–0.2M–2N is endowed with a dramatically weakened HER activity compared to $CZ_{0.7}S$–2N–0.2M. Therefore, the results displayed in this work indicate that we can optimize the capability of photocatalyst with multi-component cocatalysts by rationally regulating the coupling sequence to achieve efficient migration and separation of charge carriers.

4 CONCLUSION

In summary, homogeneous $Cd_{1-x}Zn_xS$–Ni_2P–MoS_2 hybrid nano-spheres were obtained through the ultrasonic water-bath method combined with solvothermal and electrostatic assembly processes, which exhibit outstanding photocatalytic activity and stability toward visible-light-driven H_2 evolution. Particularly, the optimized $CZ_{0.7}S$–2N–0.2M composite with 2 *wt*% Ni_2P and 0.2 *wt*% MoS_2 demonstrates the maximum HER rate of 55.77 $mmol \cdot g^{-1} \cdot h^{-1}$, exceeding that of the Pt–$CZ_{0.7}S$, $CZ_{0.7}S$–0.2M and $CZ_{0.7}S$–2N counterparts, as well as most CdS-based photocatalysts ever reported. The superior HER performance of $CZ_{0.7}S$–2N–0.2M can be attributed to the existence of abundant active sites in Ni_2P and 1T/2H MoS_2 cocatalysts and the efficient transfer and separation of charge carriers. The findings presented in this work could facilitate the development of highly-active noble-metal-free photocatalysts to achieve efficient solar conversion and utilization.

REFERENCES

(1) Xiao, M.; Wang, Z.; Lyu, M.; Luo, B.; Wang, S.; Liu, G.; Cheng, H. M.; Wang, L. Hollow nanostructures for photocatalysis: advantages and challenges. *Adv. Mater.* **2018**, 31, 1801369–5.

(2) Zhang, J.; Wang, T.; Liu, P.; Liao, Z. Q.; Liu, S. H.; Zhuang, X. D.; Chen, M. W.; Zschech, E.; Feng, X. L. Efficient hydrogen production on $MoNi_4$ electrocatalysts with fast water dissociation kinetics. *Nat. Commun.* **2017**, 8, 15437–8.

(3) Wei, Y. Z.; Wang, J. Y.; Yu, R. B.; Wan, J. W.; Wang, D. Constructing $SrTiO_3$-TiO_2 heterogeneous hollow multi-shelled structures for enhanced solar water splitting. *Angew. Chem. Int. Edit*. **2019**, 58, 1422–1426.

(4) Chen, J. Z.; Wu, X. J.; Yin, L. S.; Li, B.; Hong, X.; Fan, Z. X.; Chen, B.; Xue, C.; Zhang, H. One-pot synthesis of CdS nanocrystals hybridized with single-layer transition-metal dichalcogenide nanosheets for efficient photocatalytic hydrogen evolution. *Angew. Chem. Int. Edit.* **2015**, 54, 1210–1214.

(5) Kudo, A.; Miseki, Y. Heterogeneous photocatalyst materials for water splitting. *Chem. Soc. Rev.* **2009**, 38, 253–278.

(6) Li, Q.; Meng, H.; Zhou, P.; Zheng, Y. Q.; Wang, J.; Yu, J. G.; Gong, J. R. $Zn_{1-x}Cd_xS$ solid solutions with controlled bandgap and enhanced visible-light photocatalytic H_2-production activity. *ACS Catal.* **2013**, 3, 882–889.

(7) Song, J. G.; Zhao, H. T.; Sun, R. R.; Li, X. Y.; Sun, D. J. An efficient hydrogen evolution catalyst composed of palladium phosphorous sulphide ($PdP_{\sim 0.33}S_{\sim 1.67}$) and twin nanocrystal $Zn_{0.5}Cd_{0.5}S$ solid solution with both homo-and hetero-junctions. *Energy Environ. Sci.* **2017**, 10, 225–235.

(8) Zhang, L. X.; Pan, X. Y.; Wang, G. T.; Long, X.; Yi, Z. G. TiO_2–Ti_3C_2 composites with Pt decoration as efficient photocatalysts for ethylene

oxidation under near infrared light irradiation. *Chin. J. Struct. Chem.* **2018**, 373, 1457–1469.

(9) Osterloh, F. E. Inorganic materials as catalysts for photochemical splitting of water. *Chem. Mater.* **2008**, 20, 35–54.

(10) Chen, X. P.; Chen, W.; Gao, H. Y.; Yang, Y.; Shangguan, W. F. *In situ* photodeposition of NiO_x on CdS for hydrogen production under visible light: enhanced activity by controlling solution environment. *Appl. Catal., B-Environ.* **2016**,152, 68–72.

(11) Guan, S.; Fu, X.; Zhang, Y.; Peng, Z. *β*-NiS modified CdS nanowires for photocatalytic H_2 evolution with exceptionally high efficiency. *Chem. Sci.* **2018**, 9, 1574–1585.

(12) Tian, F. Y.; Hou, D. F.; Tang, F.; Deng, M.; Qiao, X. Q.; Zhang, Q. C.; Wu, T.; Li, D. S. Novel $Zn_{0.8}Cd_{0.2}S$@*g*-C_3N_4 core-shell heterojunctions with a twin structure for enhanced visible-light-driven photocatalytic hydrogen generation. *J. Mater. Chem. A* **2018**, 6, 17086–17094.

(13) Chang, K.; Mei, Z. W.; Wang, T.; Kang, Q.; Ouyang, S. X.; Ye, J. H. MoS_2/graphene cocatalyst for efficient photocatalytic H_2 evolution under visible light irradiation. *ACS Nano* **2016**, 8, 7078–7087.

(14) Chang, K.; Hai, X.; Ye, J. H. Transition metal disulfides as noble-metal-alternative co-catalysts for solar hydrogen production. *Adv. Energy Mater.* **2016**, 6, 1502555–21.

(15) Sun, Z. J.; Zheng, H. F.; Li, J. S.; Du, P. W. Extraordinarily efficient photocatalytic hydrogen evolution in water using semiconductor nanorods integrated with crystalline Ni_2P cocatalysts. *Energy Environ. Sci.* **2015**, 8, 2668–2676.

(16) Li, H.; Yan, X. Q.; Lin, B.; Xia, M. Y.; Wei, J. J.; Yang, B. L.; Yang, G. D. Controllable spatial effect acting on photo-induced CdS@CoP@SiO_2 ball-in-ball nano-photoreactor for enhancing hydrogen evolution. *Nano Energy* **2018**, 47, 481–493.

(17) Maitra, U.; Gupta, U.; De, M.; Datta, R.; Govindaraj, A.; Rao, C. N. R. Highly effective visible-light-induced H_2 generation by single-layer 1T-MoS_2 and a nanocomposite of few-layer 2H-MoS_2 with heavily nitrogenated graphene. *Angew. Chem. Int. Edit.* **2018**, 52, 13057–13061.

(18) Chang, K.; Hai, X.; Pang, H.; Zhang, H. B.; Shi, L.; Liu, G. G.; Liu, H. M.; Zhao, G. X.; Li, M.; Ye, J. H. Targeted synthesis of 2H- and 1T-phase MoS_2 monolayers for catalytic hydrogen evolution. *Adv. Mater.* **2016**, 28, 10033–10041.

(19) Pan, Y.; Hu, W. H.; Liu, D. P.; Liu, Y. Q.; Liu, C. G. Carbon nanotubes decorated with nickel phosphide nanoparticles as efficient nanohybrid electrocatalysts for the hydrogen evolution reaction. *J. Mater. Chem. A* **2015**, 3, 13087–13094.

(20) Eda, G.; Yamaguchi, H.; Voiry, D.; Fujita, T.; Chen, M. W.; Chhowalla, M. Photoluminescence from chemically exfoliated MoS_2. *Nano Lett.* **2011**, 11, 5111–5116.

(21) Choi, J.; Reddy, D. A.; Han, N. S.; Jeong, S.; Hong, S.; Kumar, D. P.; Song, J. K.; Kim, T. K. Modulation of charge carrier pathways in CdS nanospheres by integrating MoS_2 and Ni_2P for improved migration and separation toward enhanced photocatalytic hydrogen evolution. *Catal. Sci. Technol.* **2017**, 7, 641–649.

(22) Doktycz, S. J.; Suslick, K. S. Interparticle collisions driven by ultrasound. *Science* **1990**, 247, 1067–1069.

(23) Tehrani, A. A.; Safarifard, V.; Morsali, A.; Bruno, G.; Rudbari, H. A. Ultrasound-assisted synthesis of metal-organic framework nanorods of Zn-HKUST-1 and their templating effects for facile fabrication of zinc oxide nanorods via solid-state transformation. *Inorg. Chem. Commun.* **2015**, 59, 41–45.

(24) Hubert, C.; Naghavi, N.; Etcheberry, A.; Roussel, O.; Hariskos, D.; Powalla, M.; Kerrec, O.; Lincot, D. A better understanding of the growth mechanism of Zn(S, O, OH) chemical bath deposited buffer layers for high efficiency Cu(In, Ga)$(S, Se)_2$ solar cells. *Phys. Status Solidi A-Appl. Mat.* **2008**, 205, 2335–2339.

(25) Xie, J. F.; Zhang, J. J.; Li, S.; Grote, F.; Zhang, X. D.; Zhang, H.; Wang, R. X.; Lei, Y.; Pan, B. C.; Xie, Y. Controllable disorder engineering in oxygen-incorporated MoS_2 ultrathin nanosheets for efficient hydrogen evolution. *J. Am. Chem. Soc.* **2013**, 135, 17881–17888.

(26) Yin, X. L.; Li, L. L.; Jiang, W. J.; Zhang, Y.; Zhang, X.; Wan, L. J.; Hu, J. S. MoS_2/CdS nanosheets-on-nanorod heterostructure for highly efficient photocatalytic H_2 generation under visible light irradiation. *ACS Appl. Mater. Interfaces* **2016**, 8, 15258–15266.

(27) Chen, S. F.; Hu, Y. F.; Meng, S. G.; Fu, X. L. Study on the separation mechanisms of photogenerated electrons and holes for composite photocatalysts *g*-C_3N_4-WO_3. *Appl. Catal. B-Environ.* **2016**, 150, 564–573.

(28) Li, S. S.; Wang, L.; Li, Y. D.; Zhang, L. H.; Wang, A. X.; Xiao, N.; Gao, Y. Q.; Li, N.; Song, W. Y.; Ge, L.; Liu, J. Novel photocatalyst incorporating Ni–Co layered double hydroxides with P-doped CdS for enhancing photocatalytic activity towards hydrogen evolution. *Appl. Catal., B-Environ.* **2019**, 254, 145–155.

(29) Xu, X. J.; Hu, L. F.; Gao, N.; Liu, S. X.; Wageh, S.; Al-Ghamdi, A. A.; Alshahrie, A.; Fang, X. S. Controlled growth from ZnS nanoparticles to ZnS–CdS nanoparticle hybrids with enhanced photoactivity. *Adv. Funct. Mater.* **2015**, 25, 445–454.

(30) Zhang, X.; Li, X. H.; Shao, C. L.; Li, J. H.; Zhang, M. Y.; Zhang, P.; Wang, K. X.; Lu, N.; Liu, Y. C. One-dimensional hierarchical heterostructures

of In_2S_3 nanosheets on electrospun TiO_2 nanofibers with enhanced visible photocatalytic activity. *J. Hazard. Mater.* **2013**, 260, 892–900.

(31) Zhang, S. W.; Yang, H. C.; Gao, H. H.; Cao, R. Y.; Huang, J. Z.; Xu, X. J. One-pot synthesis of CdS irregular nanospheres hybridized with oxygen-incorporated defect-rich MoS_2 ultrathin nanosheets for efficient photocatalytic hydrogen evolution. *ACS Appl. Mater. Interfaces* **2017**, 9, 23635–23646.

(32) Zhang, G. P.; Chen, D. Y.; Li, N. J.; Xu, Q. F.; Li, H.; He, J. H.; Lu, J. M. Preparation of $ZnIn_2S_4$ nanosheet-coated CdS nanorod heterostructures for efficient photocatalytic reduction of Cr (VI). *Appl. Catal., B-Environ.* **2018**, 232, 164–174.

(33) Jiang, D. C.; Sun, Z. J.; Jia, H. X.; Lu, D. P.; Du, P. W. A cocatalyst-free CdS nanorod/ZnS nanoparticle composite for high-performance visible-light-driven hydrogen production from water. *J. Mater. Chem. A* **2016**, 4, 675–683.

(34) Gao, P.; Liu, J.; Sun, D. D.; Ng, W. Graphene oxide-CdS composite with high photocatalytic degradation and disinfection activities under visible light irradiation. *J. Hazard. Mater.* **2013**, 250, 412–420.

(35) Shi, Y.; Xu, Y.; Zhuo, S.; Zhang, J.; Zhang, B. Ni_2P nanosheets/Ni foam composite electrode for long-lived and pH-tolerable electrochemical hydrogen generation. *ACS Appl. Mater. Inter.* **2015**, 7, 2376–2384.

(36) Bu, X. M.; Wei, R. J.; Gao, W.; Lan, C. Y.; Ho, J. C. A unique sandwich structure of a CoMnP/Ni_2P/NiFe electrocatalyst for highly efficient overall water splitting. *J. Mater. Chem. A* **2019**, 7, 12325–12332.

(37) Kappera, R.; Voiry, D.; Yalcin, S. E.; Branch, B.; Gupta, G.; Mohite, A. D.; Chhowalla, M. Phase-engineered low-resistance contacts for ultrathin MoS_2 transistors. *Nat. Mater.* **2016**, 13 1128–1134.

(38) Chang, Y. H.; Nikam, R. D.; Lin, C. T.; Huang, J. K.; Tseng, C. C.; Hsu, C. L.; Cheng, C. C.; Su, C. Y.; Li, L. J.; Chua, D. H. C. Enhanced electrocatalytic activity of MoS_x on TCNQ-treated electrode for hydrogen evolution reaction. *ACS Appl. Mater. Inter.* **2016**, 6, 17679–17685.

(39) Liu, Z. P.; Gao, Z. C.; Liu, Y. H.; Xia, M. S.; Wang, R. W.; Li, N. Heterogeneous nanostructure based on 1T-phase MoS_2 for enhanced electrocatalytic hydrogen evolution. *ACS Appl. Mater. Inter.* **2017**, 9, 25291–25297.

(40) Wei, W.; Sun, K.; Hu, Y. H. An efficient counter electrode material for dye-sensitized solar cells-flower-structured 1T metallic phase MoS_2. *J. Mater. Chem. A* **2016**, 4, 12398–12401.

(41) Liu, Q.; Li, X. L.; He, Q.; Khalil, A.; Liu, D. B.; Xiang, T.; Wu, X. J.; Song, L. Gram-scale aqueous synthesis of stable few-layered 1T-MoS_2: applications for visible-light-driven photocatalytic hydrogen evolution. *Small* **2015**, 11, 5556–5564.

(42) Indra, A.; Acharjya, A.; Menezes, P. W.; Merschjann, C.; Hollmann, D.; Schwarze, M.; Aktas, M.; Friedrich, A.; Lochbrunner, S.; Thomas, A.; Driess, M. Boosting visible-light-driven photocatalytic hydrogen evolution with an integrated nickel phosphide-carbon nitride system. *Angew. Chem. Int. Edit.* **2017**, 56, 1653–1657.

(43) Cheng, L.; Xiang, Q. J.; Liao, Y. L.; Zhang, H. W. CdS-based photocatalysts. *Energy Environ. Sci.* **2018**, 11, 1362–1391.

(44) Venkateshwaran, S.; Senthil Kumar, S. M. Template-driven phase selective formation of metallic 1T-MoS_2 nanoflowers for hydrogen evolution reaction. *ACS Sustainable Chem. Eng.* **2019**, 7, 2008–2017.

(45) Geng, X. M.; Sun, W. W.; Wu, W.; Chen, B. J. M.; Al-Hilo, A.; Benamara, M.; Zhu, H. L.; Watanabe, F.; Cui, J. B.; Chen, T. P. Pure and stable metallic phase molybdenum disulfide nanosheets for hydrogen evolution reaction. *Nat. Commun.* **2016**, 7, 10672–7.

(46) Dai, D. S.; Wang, L.; Xiao, N.; Li, S. S.; Xu, H.; Liu, S.; Xu, B. R.; Lv, D.; Gao, Y. Q.; Song, W. Y.; Ge, L.; Liu, J. *In-situ* synthesis of Ni_2P co-catalyst decorated $Zn_{0.5}Cd_{0.5}S$ nanorods for high-quantum-yield photocatalytic hydrogen production under visible light irradiation. *Appl. Catal., B-Environ.* **2018**, 233, 194–201.

(47) Simon, T.; Bouchonville, N.; Berr, M. J.; Vaneski, A.; Adrovic, A.; Volbers, D.; Wyrwich, R.; Doblinger, M.; Susha, A. S.; Rogach, A. L.; Jackel, F.; Stolarczyk, J. K.; Feldmann, J. Redox shuttle mechanism enhances photocatalytic H_2 generation on Ni-decorated CdS nanorods. *Nat. Mater.* **2016**, 13, 1013–1018.

(48) Tang, W. Z.; Huang, C. Photocatalyzed oxidation pathways of 2,4-dichlorophenol by CdS in basic and acidic aqueous solutions. *Water Res.* **1995**, 29, 745–756.

(49) Wang, H. L.; Zhang, L. S.; Chen, Z. G.; Hu, J. Q.; Li, S. J.; Wang, Z. H.; Liu, J. S.; Wang, X. C. Semiconductor heterojunction photocatalysts: design, construction, and photocatalytic performances. *Chem. Soc. Rev.* **2016**, 43, 5234–5244.

(50) Huang, J. T.; Cui, C. N.; Yan, G. Y.; Xing, Y. L. Enhanced photocatalytic denitrification Rhodamine Bover In_2O_{33}/$Bi_{24}O_{31}Br_{10}$ nanocomposites under visible light irradiation. *Chin. J. Struct. Chem.* **2018**, 37, 611–616.

(51) Zhuang, T. T.; Liu, Y.; Sun, M.; Jiang, S. L.; Zhang, M. W.; Wang, X. C.; Zhang, Q.; Jiang, J.; Yu, S. H. A unique ternary semiconductor-(semiconductor/metal) nano-architecture for efficient photocatalytic hydrogen evolution. *Angew. Chem. Int. Edit.* **2015**, 54,

11495–11500.

(52) Kim, E. S.; Nishimura, N.; Magesh, G.; Kim, J. Y.; Jang, J. W.; Jun, H.; Kubota, J.; Domen, K.; Lee, J. S. Fabrication of $CaFe_2O_4$/TaON heterojunction photoanode for photoelectrochemical water oxidation. *J. Am. Chem. Soc.* **2013**, 135, 5375–5383.

(53) Li, K.; Han, M.; Chen, R.; Li, S. L.; Xie, S. L.; Mao, C. Y.; Bu, X. H.; Cao, X. L.; Dong, L. Z.; Feng, P. Y.; Lan, Y. Q. Hexagonal@cubic CdS core@shell nanorod photocatalyst for highly active production of H_2 with unprecedented stability. *Adv. Mater.* **2016**, 28, 8906–8911.

(54) Li, S.; Wang, L.; Xiao, N.; Wang, A.; Li, X.; Gao, Y.; Li, N.; Song, W.; Ge, L.; Liu, J. *In-situ* synthesis of ternary metal phosphides $Ni_xCo_{1-x}P$ decorated $Zn_{0.5}Cd_{0.5}S$ nanorods with significantly enhanced photocatalytic hydrogen production activity. *Chem. Eng. J.* **2019**, 378, 122220–11.

(55) Popczun, E. J.; McKone, J. R.; Read, C. G.; Biacchi, A. J.; Wiltrout, A. M.; Lewis, N. S.; Schaak, R. E. Nanostructured nickel phosphide as an electrocatalyst for the hydrogen evolution reaction. *J. Am. Chem. Soc.* **2013**, 135, 9267–9270.

(56) Zhang, X. H.; Li, N.; Wu, J. J.; Zheng, Y. Z.; Tao, X. Defect-rich O-incorporated 1T-MoS_2 nanosheets for remarkably enhanced visible-light photocatalytic H_2 evolution over CdS: the impact of enriched defects. *Appl. Catal., B-Environ.* **2018**, 229, 227–236.

(57) Yuan, Y. J.; Li, Z. J.; Wu, S. T. Chen, D. Q.; Yang, L. X.; Cao, D. P.; Tu, W. G., Yu, Z. T.; Zou, Z. G. Role of two-dimensional nanointerfaces in enhancing the photocatalytic performance of 2D-2D MoS_2/CdS photocatalysts for H_2 production. *Chem. Eng. J.* **2018**, 350, 335–343.